

Modelling the microstructure and computing effective elastic properties of sand core materials

Matti Schneider, Tobias Hofmann, Heiko Andrä, Philipp Lechner, Florian Ettemeyer, Wolfram Volk, Holger Steeb

Angaben zur Veröffentlichung / Publication details:

Schneider, Matti, Tobias Hofmann, Heiko Andrä, Philipp Lechner, Florian Ettemeyer, Wolfram Volk, and Holger Steeb. 2018. "Modelling the microstructure and computing effective elastic properties of sand core materials." *International Journal of Solids and Structures* 143 (February): 1–17. <https://doi.org/10.1016/j.ijsolstr.2018.02.008>.

Modelling the microstructure and computing effective elastic properties of sand core materials

Matti Schneider^{a,*}, Tobias Hofmann^b, Heiko Andrä^b, Philipp Lechner^c, Florian Ettemeyer^d,
Wolfram Volk^{c,d}, Holger Steeb^e

^aInstitute of Engineering Mechanics, Karlsruhe Institute of Technology, Kaiserstrae 10, Raum, Karlsruhe, 30676131, Germany

^bDepartment of Flow and Materials simulation, Fraunhofer Institute for Industrial Mathematics ITWM, Kaiserslautern, Germany

^cInstitute of Metal Forming and Casting, Technical University of Munich, Germany

^dDepartment of Casting Technology, Fraunhofer Research Institution for Casting, Composite and Processing Technology IGCV, Garching, Germany

^eInstitute of Applied Mechanics, University of Stuttgart, Germany

1. Introduction

Casting is a manufacturing process most often used for making complex shapes which would be either difficult or uneconomical to make by other methods (Blair and Stevens, 1995). Over 70% of all metal castings are produced with sand as the mold material (Rao, 2003).

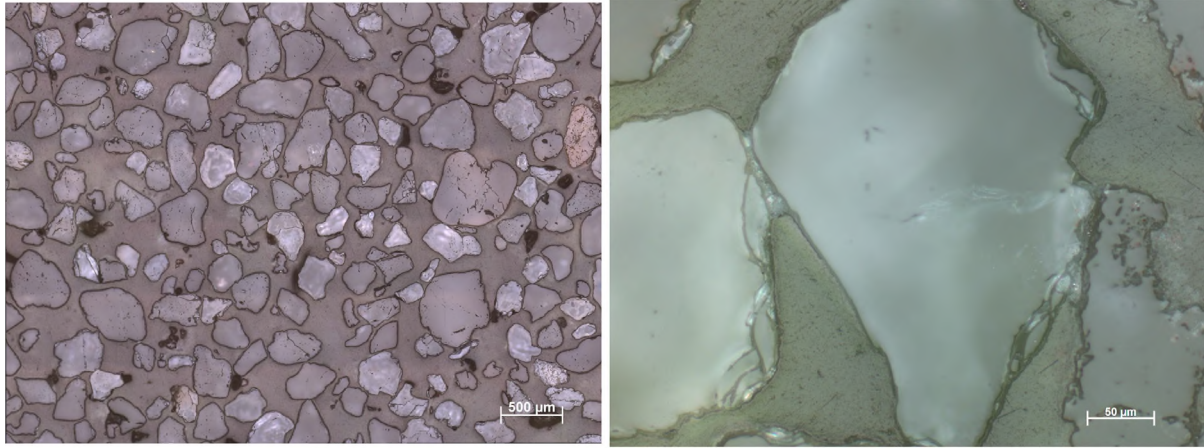
Sand cores consist of molding sand (with particular characteristics), binders, which serve to bond the sand particles together, and possible additives. The optimal mixture of these constituents is of vital importance. If the compound is not durable enough, it cannot withstand the casting process. On the other hand, it should be possible to extract the sand core after the casting without harming the metal part. Furthermore, the geometrical accuracy of the product is affected by the thermal expansion of the sand cores during metalcasting (Bakhtiyarov et al., 2007). Traditionally, optimization is carried out on a trial-and-error process, often requiring expert

knowledge not easily transferable between applications (Iden et al., 2011b).

In the last couple of years, image-based characterization techniques for materials on various scales have seen a flurry of activity (Hirano et al., 1995; Ohser and Mücklich, 2000; Cnudde and Boone, 2013). For the problem at hand, microscopic images of 2D sections of a quartz sand inorganic binder-compound are readily available, see for instance Fig. 1. For grinding and polishing purposes, the specimen was embedded with a two-component epofix resin 40200029 from Struers GmbH. Therefore, on Fig. 1(a) three phases can be distinguished: sand grains, binder and resin. The sand grains exhibit a strong variation both in terms of grain size distribution and grain shape itself. Furthermore, the sand grains are characterized by defects - both local pores and cracks are visible. However, the grinding process itself may have destructive effect on the sand grains, and the total amount of induced damage cannot be quantified from these images alone. Focussing more closely on the regions where distinct grains touch, cf. Fig. 1(b), the complexity of the sand grains' surface becomes more explicit. Furthermore, the binding bridges between the grains are readily apparent.

* Corresponding author.

E-mail address: matti.schneider@kit.edu (M. Schneider).



(a) Macroscopic overview of the compound.

(b) Binder between the sand grains.

Fig. 1. Micro-sections of the sand core material.

These binding bridges act as contact surfaces between different quartz grains, and determine the strength properties of the compound (Iden et al., 2011b). As both the 3D microstructure of these compounds can be explicitly analyzed in terms of μ XRCT images (Willsen et al., 2012), and the strength properties of individual sand grains can be measured (Wichtmann and Triantafyllidis, 2009), for instance by nanoindentation (Daphalapurkar et al., 2011), it should be possible to establish a link between these microscopic (geometric and mechanical) properties with measured/observed macroscopic properties, see for instance Caylak and Mahnken (2010) for such a macroscopic thermomechanical characterization including optical measurements.

In this work, we investigate this link by relating linear elastic properties of the constituents of the micro-scale to effective linear elastic characteristics of the compound in terms of computational homogenization on sand core microstructures. To further clarify our approach and the employed methods several comments are in order.

First, we scan three-dimensional images of the microstructure of sand core specimens using μ XRCT. However, as the densities of quartz sand, binder and additive are very similar, these phases cannot be easily segmented on the basis of the grey-scale values of the μ XRCT image. Thus, we rely on computer-generated structures to quantify the influence of both the geometric and the mechanical characteristics of the constituents, relying upon the μ XRCT images for calibration. The literature contains a number of approaches for modelling realistic sand grains and to pack those particles to high volume fraction (about 60% in volume), see Section 4 for a detailed overview. We have chosen a representation of sand particles, taken from the μ XRCT scans, by clusters of overlapping spheres (García, 2009), and to pack them by a variant of the mechanical contraction method (Williams and Philipse, 2003). The binder between the grains is introduced by mathematical morphological operations (Ohser and Schladitz, 2009). Then, incorporating a dry sieve analysis of the sand grains, statistical properties of the μ XRCT scan can be reproduced. For that purpose we model the binder as a single material, i.e. we do not distinguish the water-glass (liquid before curing) binder and the (solid before curing) additive. This approach seems imperative, as these two phases react chemically, and form a porous material with complex nanostructure (Iden et al., 2011a).

To obtain effective macroscopic mechanical properties, we rely upon the FFT-based computational homogenization technique (Moulinec and Suquet, 1994; 1998; Willot, 2015; Schneider et al.,

2016b; 2016a). For the elastic bulk properties of the quartz grains, literature values are available. However, measuring the elastic properties of the binder is difficult, and subject of current research. Thus, we perform a parameter study to quantify the influence of the elastic properties of the binder. Although precise elastic properties of the constituents are not directly available, it is easy to identify a plausible range of those characteristics. Plugging these into the simulations permits us to identify a range of computed effective elastic constants. These conform well to P-wave measurements of bar-shaped specimens.

This work is organized as follows. Section 2 introduces the used materials, their processing, and collects macroscopic measurements of compound, for instance the density and the P-wave modulus. Section 3 elaborates on the μ XRCT analysis. The generation of the digital microstructures is discussed in Section 4. Our efforts culminate in Section 5, where effective elastic properties are computed, providing a sensitivity analysis of all relevant geometrical and material parameters.

2. Experimental data

2.1. Used materials and material properties

For this work, quartz sand Haltern H32 from Quarzwerke with a mean grain size of $320\mu\text{m}$ served as our moulding sand. Fig. 2(a) shows the results of a corresponding sieve analysis at 50% relative humidity. The number of bins (and their size) was taken from the data sheet of the material. To convert a grain size distribution in terms of weight into a grain size distribution in terms of number percent our workflow is as follows. We assume that in each bin the number of particles is uniform with yet to be determined number of particles in the bin - this assumption simplifies the drawing of random numbers according to a given distribution. We consider our approach superior to fitting the parameters of a given distribution to the bins, because for the that approach the error does not become infinitesimal if the width of the bins becomes infinitesimal too. To determine the unknown particle numbers we transform this distribution to a distribution of particle volumes. Here, we assume that there is a functional relationship

particle size \mapsto particle volume of the form $r \mapsto cr^3$

where c is some (unimportant) constant. Then, we determine the particle number per bin from the relative volume fraction per bin (which we consider to equal the relative mass fraction per bin, as given in the grain size distribution).

Table 1

Variation of parameters for ten produced bar-shaped specimens in the form mean value \pm standard deviation.

Length [mm]	Width [mm]	Height [mm]	Weight [g]	Density [kg/m ³]
173.36 \pm 0.07	22.83 \pm 0.06	22.85 \pm 0.09	140.90 \pm 0.67	1558.08 \pm 8.98

Table 2

Solid volume fractions of the phases involved.

	Sand	Waterglass	Additive	Binder	Composite
solid volume fraction [%]	57.6	0.47	0.90	1.37	58.96

Clearly, our approach is defective because two particles which have equal weight according to a sieve analysis may not have the same particle size (for instance, in terms of the minimal bounding sphere), unless both particles are known to have equal shape (i.e. differ only by a rigid body motion). The result can be seen in Fig. 2(b).

For the following experiments bar-shaped specimens with a length of 170 mm and a quadratic cross section with 22.4 mm edge length and cylindrical specimens with a diameter of 50 mm and a height of 50 mm were produced in a core blowing process. Therefore, 50 kg of quartz sand and 2% (mass) of waterglass (sodium silicate, Inotec EP 4158, in a wet state) and 1.6% (mass) additive (Inotec Promotor TC 4500), which we henceforth will call binder, were mixed with a Loramendi blade mixer. The core blowing process was carried out on a Loramendi Core Blowing Machine SLC2-25L. The shooting head, shooting nozzles and sand funnel were water-cooled. The core box tool was heated up by oil to a temperature of 155°C. The specimens were blown with a pressure of 5.5 bar for 2 s. Subsequently, the specimens were gassed with hot air (220°C) for 15 s. Afterwards, the solid sand specimens are stored for 24 h in a Memmert HPP 110 climate chamber with a temperature of 20°C and a relative humidity of 20%. Microscopic sections of the dried compound are shown in Fig. 1.

To quantify the variation of the specimen dimensions and the associated density, ten bars were produced as described. Table 1 lists the mean values and corresponding standard deviations. The dimensions of the specimens were slightly larger than intended. However, the variation of these lengths is negligible. The mean density was determined as 1558 kg/m³, with about 0.5% standard deviation. Thus, we conclude that the density of the produced specimens is reproducible with high accuracy.

To determine the volume fractions of the quartz sand and binder phases within the compound, we relate the composite density with the densities of quartz (2650 kg/m³, Anthony, 1990), the density of (dry) waterglass (2610 kg/m³, Greenwood and Earnshaw, 1997) and the density of the additive (which we consider as sodium oxide with a density of 2270 kg/m³) to the density of the compound. At this point it is important to note that during the drying process the waterglass loses between 50% and 70% of its mass because of vaporization, see chapter 3 in Polzin's book (Polzin, 2012). Assuming 60% mass loss we consider only 0.8% mass of (dry) waterglass, and 1.3% of additive (both percentages in terms of mass relative to the mass of quartz sand). The respective solid volume fractions can be computed, cf. Table 2. We see that the sand is highly densified, and the binder volume fraction is very small compared to the volume fraction of quartz sand.

2.2. Measuring the *P*-wave modulus

The mechanical properties of the binder strongly depend on the humidity. At room temperature, the binder (and, thus, the compound) exhibits an almost perfectly brittle behavior. For higher moisture, the mechanical behavior becomes more ductile. For large

atmospheric humidity, this effect may even lead to a destabilization of the compound, i.e. the compound loses its form and falls apart.

Even under stable environmental conditions the elastic characterization of the sand core remains challenging, as the compound exhibits an almost perfectly brittle behavior with a hardly recognizable elastic phase. In particular, for standard mechanical tensile tests the clamping conditions strongly determine the measured elastic moduli.

Similar, but less severe, complications arise for three- and four-point bending experiments. Griebel and co-workers (Griebel et al., 2016) determined the flexural modulus of the bar-shaped specimens described above with three distinct methods: the classic way based on first order beam theory and two optical techniques. They report that the classic way leads to erratic and inconsistent results, whereas the optical techniques proved more reliable. Unfortunately, the results reported in Griebel et al. (2016) do not directly apply to our case, as they used quartz sand H35, which is coarser than the quartz sand H32 we used in our investigations.

The problems discussed in the preceding are well-known in the community investigating the mechanical properties of cementous materials or rocks. To measure the elastic properties of the materials it seems imperative to measure the speed of propagation of elastic waves in these media (Ledbetter, 1981).

We performed ultrasound through-transmission tests to obtain the *P*-wave velocities of the material. In contrast to mechanical (deformation) tests, the amplitudes of pressure waves are small and, therefore, do not destruct the sample. The *P*-wave modulus *H* will be obtained directly from the experimentally determined Time-of-Flight (ToF) Δt through

$$c_p = \Delta l / \Delta t \quad \text{with} \quad H = c_p^2 \rho.$$

The density ρ of the sample is derived through measurements of the total mass of the sample *M* and the related sample volume *V*, i.e. $\rho = M/V$. The speed of the compressional wave is given by c_p while the length of the sample is given by Δl .

The experiment is based on a classical ultrasound through-transmission setup for high-attenuating (granular) materials, cf. Güven et al. (2017). Therefore, two (identical) contact transducers are manually fixed on two sides of the sample. To improve the quality of the signal transferred from the transducers to the sample, a silicon rolling bearing grease (Unisilikon, TK 44 N3, Klüber Lubrication) is used as coupling medium. In the present case, classical water-based contact gels cannot be applied, w.r.t. the water-solubility of the sample.

The electrical high-voltage square wave pulse (amplitude 400V) is generated by a square wave pulser (Olympus 5077PR). Two identical 2 MHz broadband piezoelectric transducers (N210PL, Doppler Electronic Technologies) are applied to transform the electrical signal into a mechanical source and vice versa (transmitter and receiver). The averaged (mean value of 256 wave forms) low-voltage signal acquired by the receiver is pre-amplified (Olympus 5077PR), low-passed filtered and digitized by a high-resolution 14bit digi-

Table 3
Rise time measurements for the bar shaped sand core specimens.

	Rise time [μ s]	Length [mm]	H [GPa]	E [GPa]
measurement 1	9.964	22.9	8.31	7.73
measurement 2	9.873	22.9	8.27	7.69
measurement 3	10.240	22.9	7.87	7.32
measurement 4	10.190	23.0	8.01	7.45
average \pm stdev	10.06 \pm 0.15	22.925 \pm 0.04	8.115 \pm 0.18	7.55 \pm 0.17

tal storage oscilloscope (Picoscope 5444B). The digitized wave form is transmitted to a PC via USB, cf. Fig. 3. In a subsequent post-processing step, the digitized wave form is analyzed and the ToF as well as the P -wave modulus H is derived. In the present ultrasound tests, we have not investigated the properties of shear waves. For the solid-like samples under investigation S -wave contact transducers are complicated to couple to the surfaces of the sample. Nevertheless, a combination of P -wave contact transducers and S -wave bender elements (Lee and Santamarina, 2005) will be investigated in the future in order to directly obtain both elastic parameters (e.g. K and G) of the isotropic medium.

The corresponding Young's modulus E can be computed by

$$E = H \frac{(1 + \nu)(1 - 2\nu)}{1 - \nu}$$

if we know Poisson's ratio of the material. For the following, we assume a Poisson's ratio of $\nu = 0.17$, which corresponds to quartz glass. The results of Section 6 will show that this choice is reasonable. The measurements shown in Table 3 are consistent with the values obtained by Griebel et al. (2016), where two different optical methods were used to measure a modulus of elasticity of 7.02 ± 0.45 GPa and 7.37 ± 0.70 GPa, respectively.

3. Micro-computed tomography analysis

For the μ XRCT scan, a cylinder-shaped specimen was core-blown at the Institute of Metal Forming and Casting in Garching as described in Section 2.1. A small cuboid sample was sawed and analyzed with the μ XRCT scanner at Fraunhofer ITWM and a voxel resolution of $4\mu\text{m}$ and $2787 \times 2787 \times 2267$ voxels, cf. Fig. 4. The grey value image was post-processed with the Fraunhofer ITWM software MAVI, and segmented with the help of GeoDict (Geo, 2017) based upon the global threshold provided by Otsu's method (Otsu, 1979). The binarized image was subsequently cropped and cleansed from voxel artifacts, resulting in a $1500 \times 1500 \times 2100$ voxel image with a total solid volume fraction of 60.23%.

The total volume was divided into $4 \times 4 \times 4 = 64$ subvolumes, each with $375 \times 375 \times 525$ voxels. In Fig. 5(a) the distribution of the volume fraction in these 64 subvolumes is shown. Most of the samples are concentrated in the region between 60% and 62% volume fraction. However, there are notable anomalies with very low solid volume fractions - there is one sample with 54.89% solid volume fraction, for instance. Apparently, there is a strong variance in the local solid volume fraction.

In the binarized image, the porosity of the sand grains on a scale of a few micron is visible, but not correctly resolved with our resolution. An attempted μ XRCT-scan with a resolution of $1\mu\text{m}$ was tainted with visual artifacts, and we decided to stay with the $4\mu\text{m}$ scans, i.e. to treat the sand grain on the $4\mu\text{m}$ scale as a homogeneous medium. For that reason, the small scale porosity needed to be cleansed, see Fig. 6 for a 2D view of a small portion of the full μ XRCT image. On first sight, see Fig. 6(a), the small scale pores are not visible. However, inverting the structure (Fig. 6(b)) and highlighting the pores (Fig. 6(c)) clarifies the situation. For the entire binarized μ XRCT-image 0.58% of the volume are occupied by such

small scale pores. Cleansing them, and inverting the structure finally gets rid of the small scale pores.

4. Microstructure generation

Computer-generated microstructures are vital for computational homogenization. Even when μ XRCT-scans are available, the resulting microstructures never exhibit the degree of homogeneity necessary for computational homogenization. Generated microstructures enable prescribing various microstructural parameters and help identifying those moduli which dominate the material response of the composite. Regularly, astonishingly small volume elements turn out to be representative for the effective mechanical behavior.

For the sand core microstructure, our generation strategy follows a two step procedure. First, the sand grains are inserted into the volume element. Afterwards, the binding agent is added. Both procedures should take into account the correct volume fractions according to Table 2, i.e. $\approx 58\%$ sand grains and $\approx 1.4\%$ binder, which means that the sand grains are packed close to their maximal packing (in terms of isotropic jamming) and only a tiny portion of binder is added. The procedure should furthermore take into account the sand grains' shape and the results of the sieve analysis. Last but not least, the resulting structure should exhibit the "correct" mechanical behavior if the respective phases are furnished with suitable material laws. In particular, the structure should be stable (i.e. in a jammed state) in the sense that it is connected and supports itself.

A variety of approaches for modelling sand grains beyond spherical shapes can be found in the literature, most prominently by polyhedra (Cundall, 1988a; 1988b; Höhner et al., 2010), but also in terms of polar representations (Hogue and Newland, 1994), discrete function representation (Williams and O'Connor, 1999), Radon transform-based modeling (Leavers, 2000), super-quadratics particles (Leavers, 1998), spherical harmonics (Mollon and Zhao, 2013), level set functions (Houlsby, 2009; Stafford and Jackson, 2010; Sonon et al., 2012), binarized images (Jia et al., 2002) and clusters of overlapping (Favier et al., 1999; Ferrellec and McDowell, 2008; Garcia et al., 2009; Barrios et al., 2013) and non-overlapping spheres (O'Sullivan, 2011; Rowe et al., 2005). Concerning particle packing possible algorithms to reach high solid volume fractions include the Lubachevsky-Stillinger algorithm and its descendents based on DEM (Stillinger and Lubachevsky, 1993; Maggi et al., 2008; Stafford and Jackson, 2010), sedimentation methods (Bennet, 1972; Nolan and Kavanagh, 1992; Coelho et al., 1997; Heitkam et al., 2012), the Torquato-Jiao method using ideas from linear programming (Torquato and Jiao, 2010; Marcotte and Torquato, 2013), Monte-Carlo-move schemes (Torquato and Jiao, 2009; Damasceno et al., 2012; Henzie et al., 2012), level-set assisted RSA (Sonon et al., 2012) and the mechanical contraction method of Williams and Philipse (2003). These methods differ in their effectiveness when non-spherical particles are taken into account. Thus, the choices how to describe the sand grain and how to pack it afterwards are inherently linked.

In this work, we choose to represent the sand grains as clusters of overlapping spheres, and to use a variant of the mechanical

Table 4Particles extracted from μ XRCT image.

	Resolution	Number of spheres
particle 1	140 × 140 × 100	280
particle 2	100 × 100 × 100	280
particle 3	125 × 125 × 175	284
particle 4	150 × 110 × 150	284
particle 5	175 × 175 × 175	287

contraction method of Williams–Philipse for the compaction of the granular medium. The chosen methods convince with their computational efficiency. For DEM simulations, the bumpy surfaces of the sphere cluster particles fail to mimic the friction behavior of the “real” particle, see for instance Höhner et al. (2010). For our application, due to the presence of the binder inter-particle friction is neglected.

4.1. Extraction of volume images of representative sand grains

To get insight into the real grain shapes we rely upon the μ XRCT-scans of Section 3. Unfortunately, the sand grains are connected by the binding agent, and both phases cannot be accurately segmented on the basis of the grey-scale images of the μ XRCT scans. Thus, we make use of μ XRCT analysis software, more precisely, we invert (a few samples of) the binarized μ XRCT image, i.e. we exchange the air and solid phases, and identify pores by the watershed transform (Chapter 4 in Ohser and Schladitz, 2009), implemented in GeoDict (Geo, 2017). Most of the identified “pores” cannot be used further. However, we successfully identified five sand grain shapes, depicted in Fig. 7, with their original resolution and scale. Some of the binding bridges are still visible.

These five particles serve as the basis of our further investigations. Even on first sight, their complexity becomes apparent.

4.2. Conversion into a cluster of overlapping spheres

For packing particles with complex shapes, efficient collision detection typically determines the overall performance of the algorithms, in particular if non-convex particles are taken into account. We decided to represent a given particle as a cluster of overlapping spheres, where collision detection is simple, possibly at the expense of a large number of spheres necessary to describe the particle. For conversion, we use the COS algorithm of Garcia, described in chapter 3 of his PhD thesis (Garcia, 2009), see also Ferrellec and McDowell (2008) and Li et al. (2015) for similar approaches. COS is a Greedy algorithm, which adds spheres completely contained in the given volume successively, with the total covered volume serving as the objective in question. Fig. 8 illustrates the COS algorithm. A high number of spheres is needed to accurately model the particle. Following Garcia, we choose 90% volume coverage as the termination criterion. The number of spheres which are necessary is summarized in Table 4, and varies between 280 and 287. If we interpret this number to measure the degree of non-sphericity of a particle, apparently for all of these five particles the degree of non-sphericity is very similar. Once the particle cluster is identified, it is saved in a text file, including the volume, the center of mass, the inertia tensor, a minimal bounding sphere, and all the individual spheres. This “template” can be re-scaled w.r.t. the centroid to generate particles of the same shape, but different size, enabling an accurate recovery of the sieve analysis. We use the diameter of the bounding sphere to sort the particle into the correct bin for sieve analysis. Due to the non-sphericity, the generated particles are smaller than their μ XRCT counterparts. This can be seen in Fig. 13. However, as computational homogenization of elasticity is size-independent, the mean grain size does not enter the effective

elastic constants. Instead, only the degree of non-uniformity of the size distribution enters. To keep the generated volume elements as small as possible, we do not rely upon drawing the particle sizes randomly from the pre-selected distribution. Indeed, this type of Monte Carlo sampling the relevant quantities only converge as $N^{-\frac{1}{2}}$ in the number of particles N . Thus, to obtain a relative error of 1% on the order of 10,000 particles are required on average. To reduce the number of necessary particles we sample the particle size distribution by the Sobol sequence (Sobol, 1967), starting with the 101st element of the sequence. This type of low-discrepancy sequence (Dick and Pillichshammer, 2010) leads to a convergence order of $1/N$, reducing the number of necessary particles to obtain a relative error of 1% to the order of 100.

4.3. Grain packing by the mechanical contraction method

Suppose we wish to pack N particles, each represented by a sphere cluster. For each index $i \in \{1, 2, \dots, N\}$ the sphere cluster is described by its centroid c_i , n_i vectors v_{ia} and radii r_{ia} , where n_i denotes the number of spheres within each cluster. As a set, the i th cluster is given as

$$\{x \in \mathbb{R}^3 \mid \|x - c_i - v_{ia}\| \leq r_{ia} \text{ for some } a \in \{1, 2, \dots, n_i\}\},$$

where $\|\cdot\|$ denotes the Euclidean distance. We wish to pack the sphere clusters in a cubical box $Y = [0, L]^3$ with periodic boundary conditions. The mechanical contraction method, originally formulated for spheres and spherocylinders (Williams and Philipse, 2003), starts with an initial configuration of particles (overlapping or non-overlapping) with a very low volume fraction. Then, two different phases are executed in an alternate fashion:

1. mechanical contraction
2. overlap removal

For the mechanical contraction, the box $Y = [0, L]^3$ (and the centroids of the particles inside) is re-scaled by a factor $\rho \in (0, 1)$, s.t. the new cell is given as $Y' = [0, L']^3$ with $L' = \rho L$. As only the centroid, but not the size of the particles are re-scaled, the volume fraction is increased, possibly at the expense of generated induced overlap. The non-interpenetrability condition of the N particles in the box Y (where we drop the prime for notational clarity) is classically formulated in terms of inequalities

$$\begin{aligned} \text{dist}_Y(c_i + v_{ia}, c_j + v_{jb}) &> r_{ia} + r_{jb} \quad \text{for all } 1 \leq i < j \leq N, \\ a \in \{1, 2, \dots, n_i\}, b \in \{1, 2, \dots, n_j\}, \end{aligned} \quad (1)$$

where dist_Y stands for the periodic Euclidean distance w.r.t. the cell Y , which we rewrite in the form of an equality

$$\begin{aligned} \max \left(0, \max_{1 \leq a \leq n_i, 1 \leq b \leq n_j} [r_{ia} + r_{jb} - \text{dist}_Y(c_i + v_{ia}, c_j + v_{jb})] \right) &= 0 \\ \text{for all } 1 \leq i < j \leq N. \end{aligned}$$

To remove possible overlap, the mechanical contraction method mimicks a penalty method (without objective function) and seeks a minimizer of the associated energy

$$f(c_1, \dots, c_N, R_1, \dots, R_N) = \sum_{1 \leq i < j \leq N} \delta_{ij}^2,$$

where δ_{ij} is a shorthand notation for

$$\delta_{ij} = \max \left(0, \max_{1 \leq a \leq n_i, 1 \leq b \leq n_j} [r_{ia} + r_{jb} - \text{dist}_Y(c_i + R_i v_{ia}, c_j + R_j v_{jb})] \right)$$

and the $R_i \in SO(3)$ are rotations. f is a continuously differentiable function of its arguments, and $f = 0$ precisely if the inequality constraints (1) are satisfied. To minimize f , Williams–Philipse propose

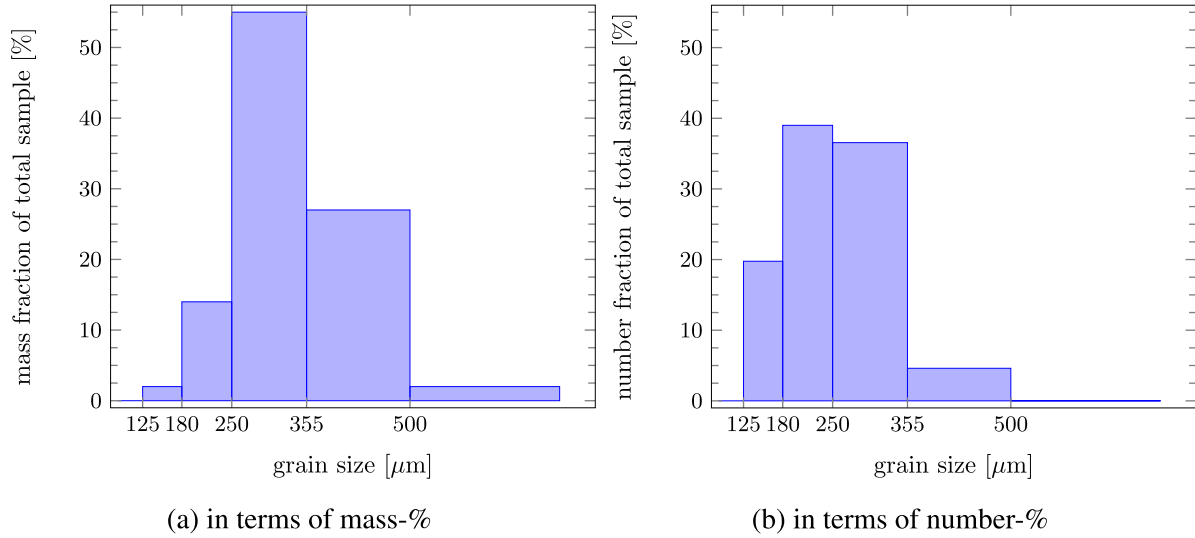


Fig. 2. Grain size distribution for the used Quartz sand.

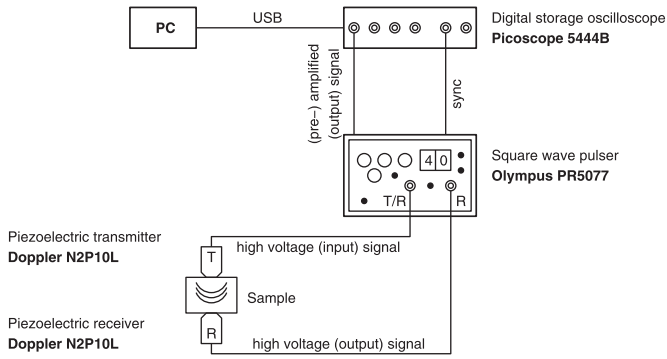


Fig. 3. Schematic of the P -wave measurement device.

cle 1 and the sieve analysis depicted in Fig. 2, a packing ratio of about 68% solid volume can be reached cf. Fig. 9, where the volume fractions in the “mechanical contraction” phase are increased by 0.25% volume at each step.

However, for the core blowing application, no such strict jamming is needed. We use the sequence {10, 20, 30, 40, 45, 50, 55, 60, 61} of volume fractions (in %) to obtain our packings. Then, for the obtained packings each particle is re-scaled w.r.t. its centroid in such a way that the total volume fraction equals 58.16%. Packing to higher volume fractions than 61% does not affect the effective properties after rescaling, but takes much more computing time. Notice that we do not directly pack to 58.16%. For such a non-rescaled pack some particles are touching, and others are much farther apart. In particular, the variance of the effective properties is extremely increased. The latter phenomenon can be easily seen already for monodisperse sphere packings, where particle collections with higher packing density (subsequently rescaled) turn out to be much more homogeneous and reliable for our application.

4.4. Particle coating and adding binder

Suppose a granular packing of the desired volume fraction is reached. Subsequently, we wish to add the binding agent in such a

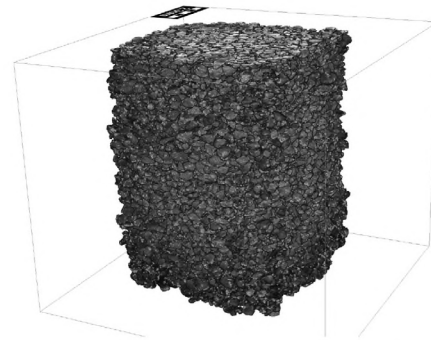
a gradient method with step size $h \leq 0.5$, i.e. in our context, the variables c_i and R_i are updated according to the formulae

$$c_i \leftarrow c_i - h \nabla_{c_i} f \quad \text{and} \quad R_i \leftarrow \exp(-h \nabla_{R_i} f) R_i,$$

where \exp denotes the matrix exponential. Formulae for the gradient ∇f are easily computed. The method just described enables computing random jammed packings of sphere clusters. For parti-

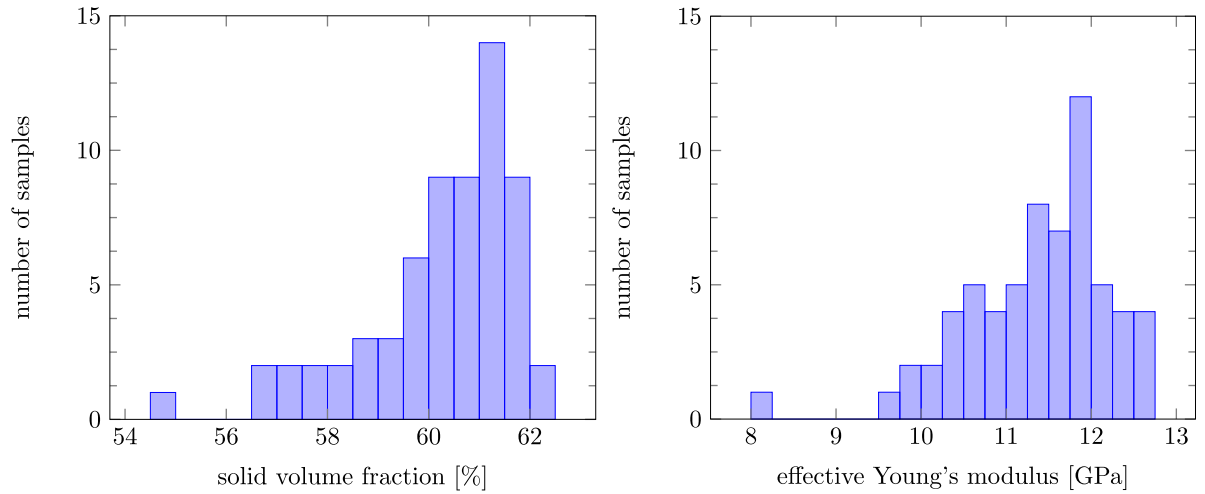


(a) Cylinder specimen, sawn into pieces.



(b) Surface rendering of the μ XRCT-scan

Fig. 4. Preparation of a cuboid sample for μ XRCT-scanning and a surface view of the μ XRCT scan.



(a) Histogram of the solid volume fraction distribution (b) Effective Young's moduli for $E = 100\text{GPa}$, $\nu = 0.17$

Fig. 5. Distribution of volume fractions and computed Young's moduli (see Section 5) for the 64 subsamples of the μXRCT images.

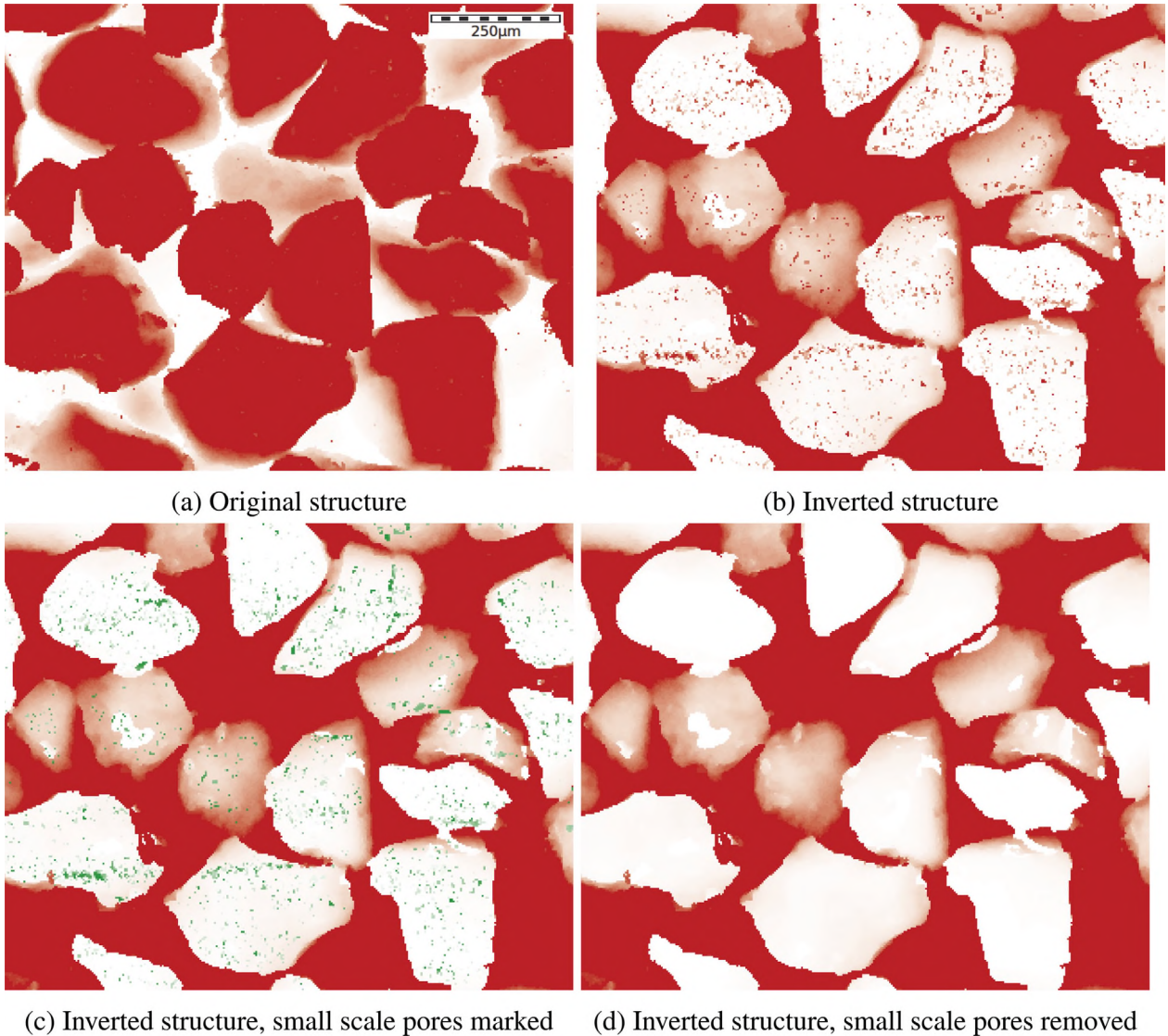


Fig. 6. Removing the small scale pores from the μXRCT image.

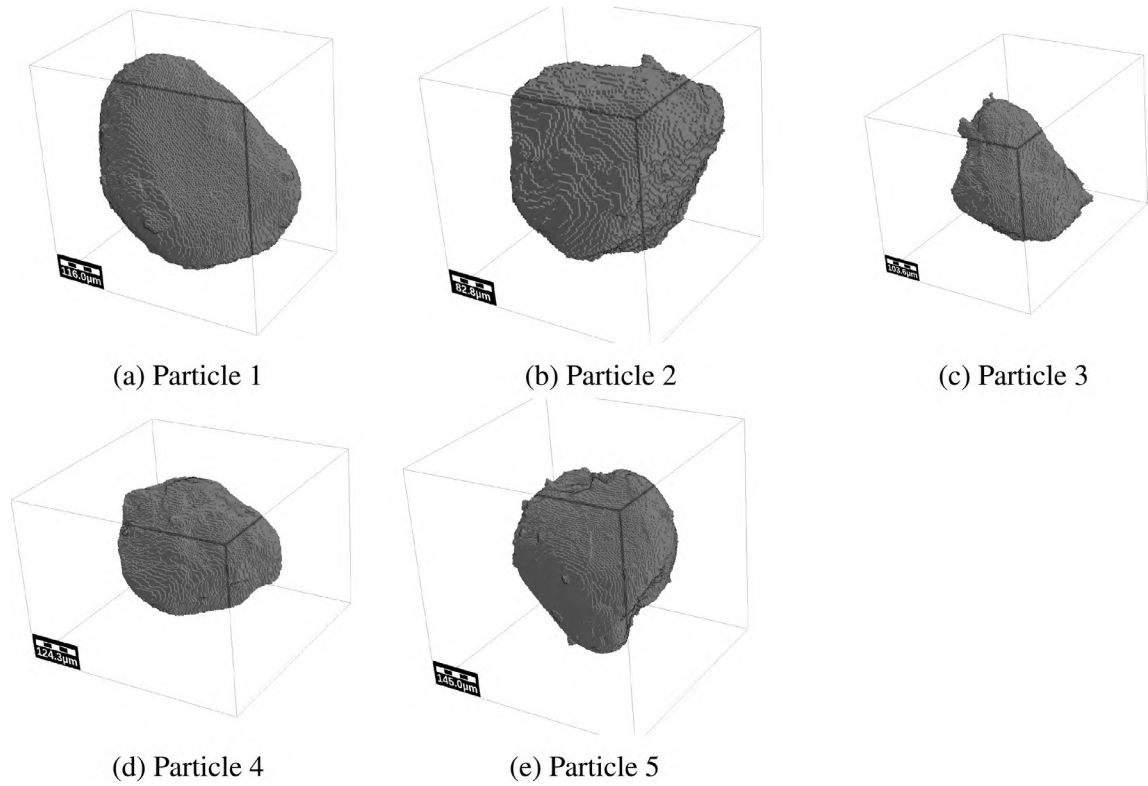


Fig. 7. Sand particles, manually identified from the μ XRCT image.

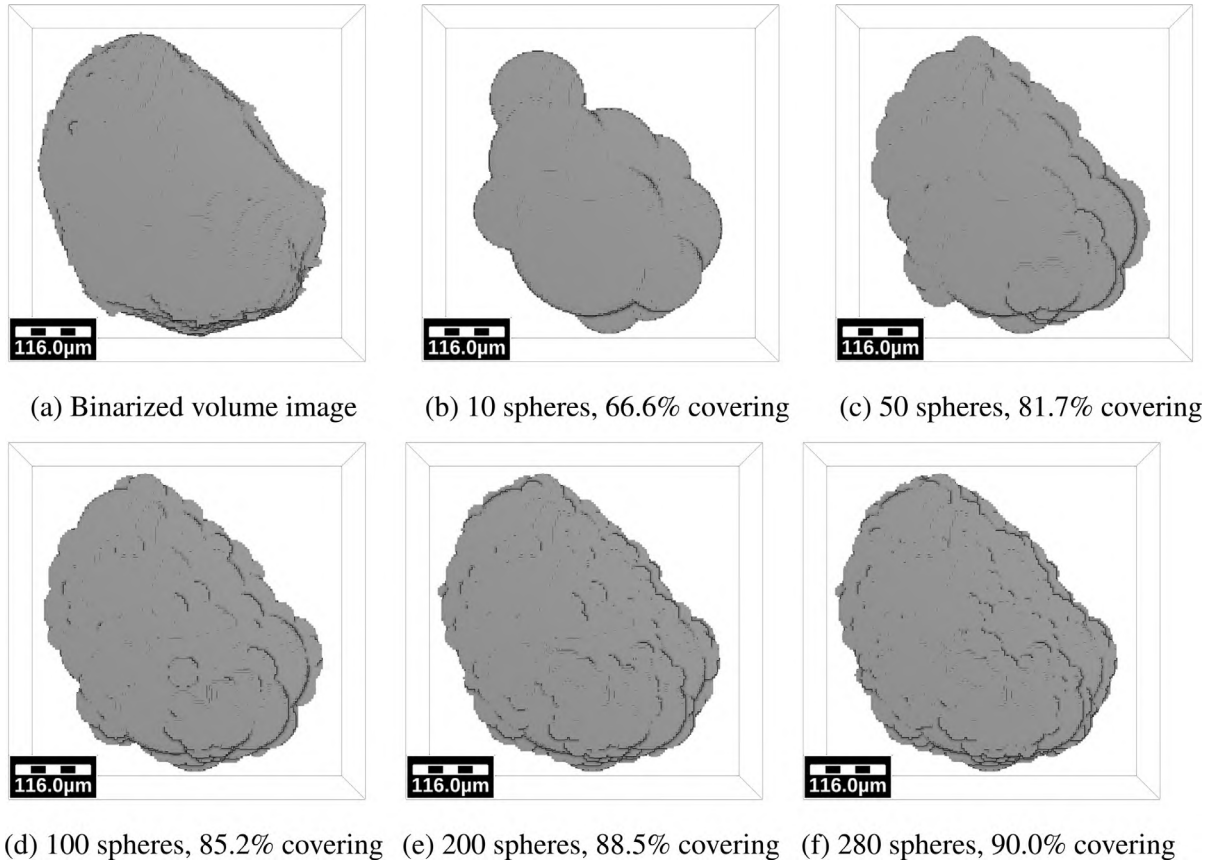


Fig. 8. Illustration of the COS method for particle 1, including the number of spheres and the covered volume.

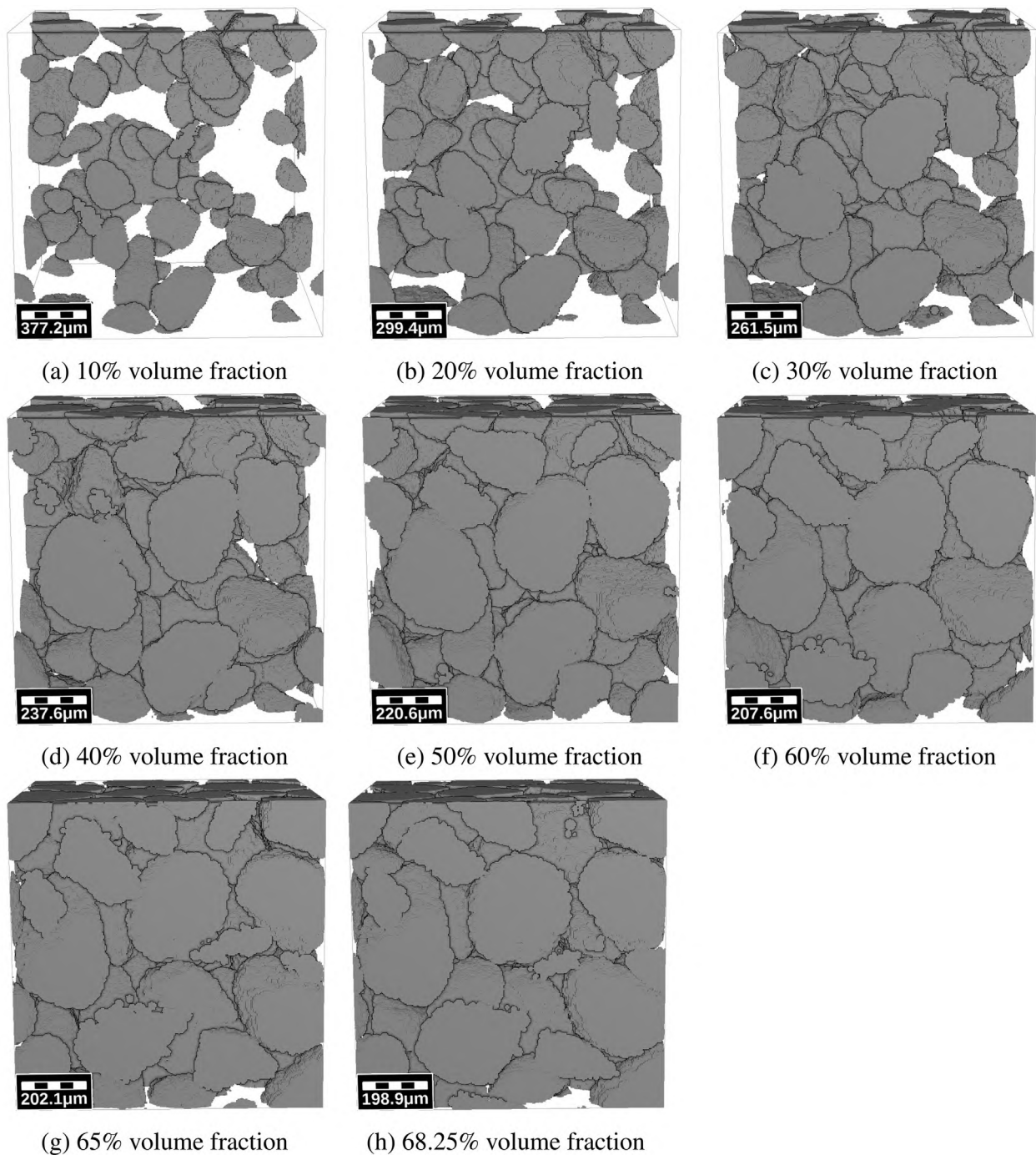


Fig. 9. Illustration of different compactifications obtained by the mechanical contraction method for particle 1, 64 sand grains and the sieve analysis of Fig. 2.

way that binding bridges form a load-bearing structure. In contrast to the preceding algorithms, which were based on an analytical description of the granular packing, from this part on we change to a voxel description of the microstructure, i.e. a binarized representation on a periodic cubical grid.

To add binder, we rely upon the AddBinder function available in Geo (2017), which implements techniques of mathematical morphology: dilation and erosion by spheres, see Chapter 4 in Ohser and Schladitz (2009). For dilation and erosion spheres of different radii are used. These radii are adjusted iteratively until the desired volume fraction of binder is reached. This AddBinder technique is used to connect different particles, as will be shown in the next paragraph. However, for sphere clusters, it leads to an un-

desired ancillary effect: binder is also added to each particle, filling the ridges between the overlapping spheres, cf. Fig. 10. Thus, we cannot precisely control the volume fraction of the binder contributing to the load-bearing capacity.

To overcome this limitation we insert an additional step: we coat each particle individually, disregarding the other particles. This process is illustrated in Fig. 11. Adding 5% of the particles volume as binder closes the ridges of the sphere cluster, cf. Fig. 11(c). Interestingly, the resulting coated particle resembles closely the μ XRCT image we started out with, compare Fig. 11(e) and 11(a). We experimented with different levels of added binder. Adding 10% of the particles volume introduces cusps not present for the original article, cf. Fig. 11(d).

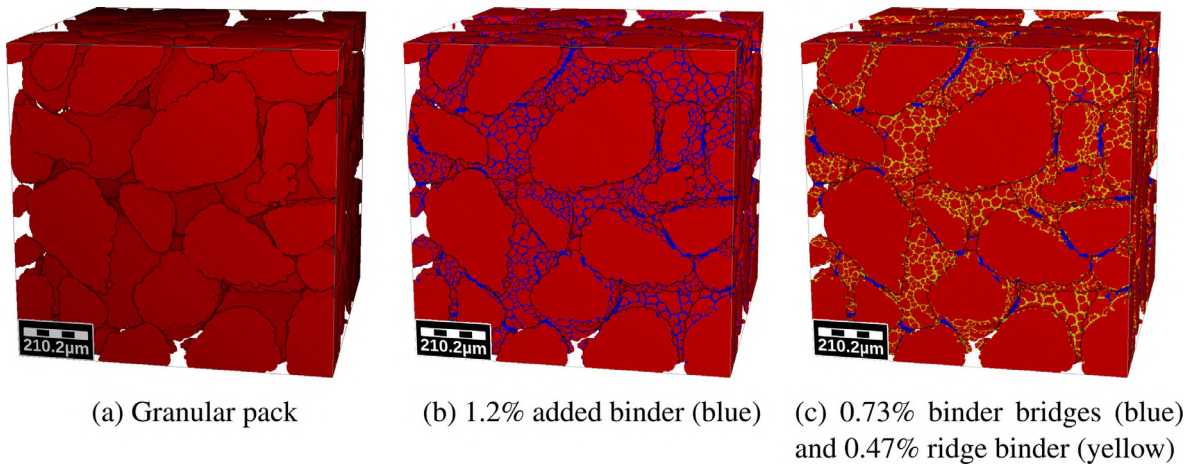


Fig. 10. Undesired effects of naively adding binder: binder is distributed into the ridges on the particles' surface, reducing the volume fraction of the binder bridges significantly.

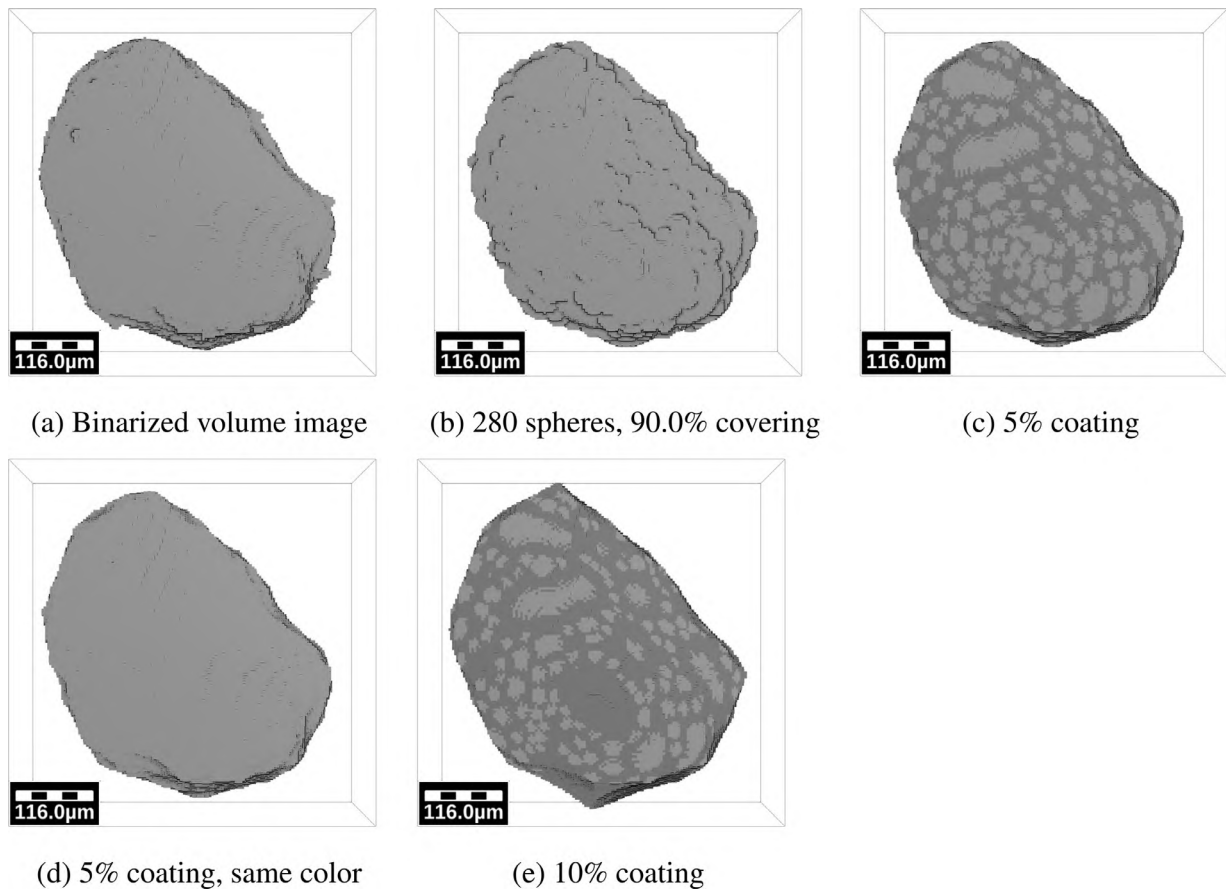


Fig. 11. Illustration of particle coating. We compare the original volume image with the sphere cluster representation and 5% as well as 10% added coating, respectively. The dark gray in (c) and (e) shows the coating added to the light grey sphere clusters. Figs. (c) and (d) show the same particle, but in (d) the coating is also shown in light grey to better compare it to (a).

In order to have the correct volume fraction taking into account the coating procedure, before coating the particles are shrunk by a factor of 1/0.95 (w.r.t. their centroid). As each particle is coated individually, overlap between different particles might occur. However, for all the structures used in this article, the overlapping volume was below 0.01%. Thus, we do not consider this a problem.

In a last step, binder is added to the coated granular pack, as shown in Fig. 12. Although the deviations are not as large as before, it is still not always possible to reach the prescribed binder

content exactly. This is due to the voxel discretization based morphological operation used in the AddBinder procedure of GeoDict. The radii of the spheres used for the dilation and erosion operations can effectively only be a multiple of the voxel resolution. Thus, the resulting binder volume fractions are quantized, which is problematic in particular for very low binder volume fractions, i.e. below 2%. To adapt to this situation, we plot the computational results as functions over the reached volume fractions, and select the “best” microstructures a posteriori.

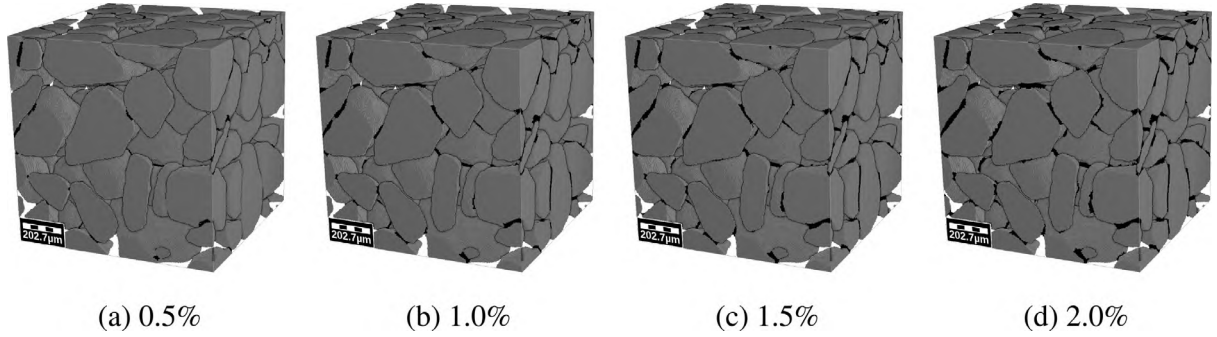


Fig. 12. Adding binder to the coated granular pack, with different volume fractions.

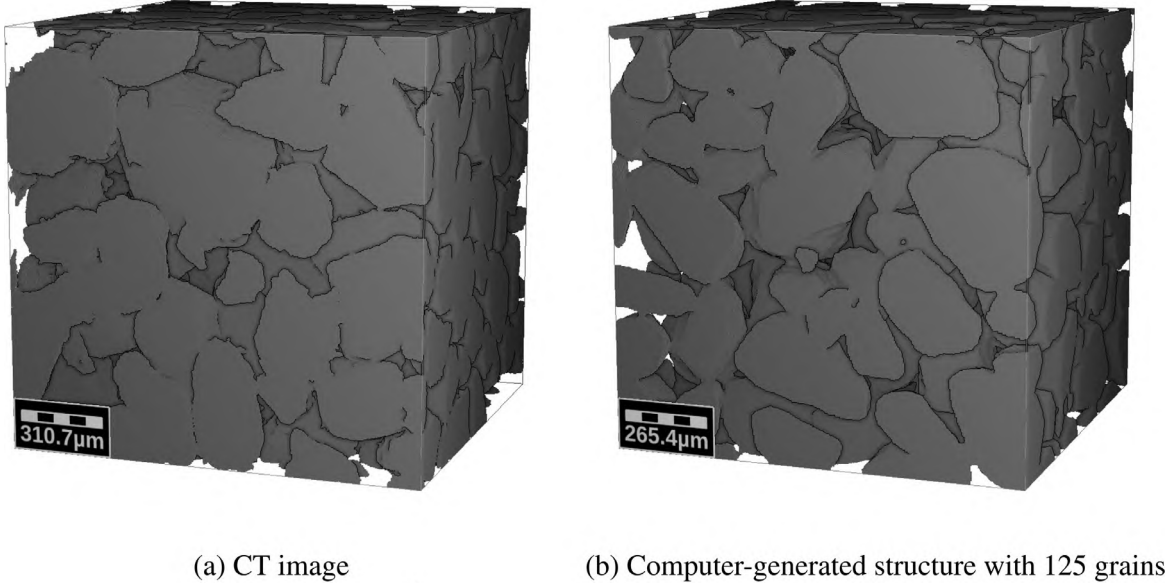


Fig. 13. Visual comparison of a 375^3 subsample of the μ XRCT image and a computer-generated structure.

5. Effective elastic properties

5.1. Setup, methods and software

To compute effective elastic properties of microstructures we use computational homogenization (Holister and Kikuchi, 1994). As our microstructures are periodic and given on a voxel grid, we rely upon a variant of the FFT-based homogenization method, introduced by Moulinec and Suquet (1994, 1998). The original method could not handle porous microstructures, directly. However, this limitation could be overcome by a change of discretization (Willot, 2015; Schneider et al., 2016b; 2016a). For the problem at hand, we use a discretization on a staggered grid (Harlow and Welch, 1965; Gerritsma, 1996; Schneider et al., 2016b), solved by an FFT-preconditioned conjugate gradient method (Zeman et al., 2010; Brisard and Dormieux, 2010; 2012), implemented in the Fraunhofer ITWM software FeelMath (Finite, 2017).

For linear elastic homogenization, 6 load cases, corresponding to 3 tensile and 3 shear loadings, are computed. The resulting effective stresses are combined into an effective elastic tensor \mathbb{C}^{eff} . We seek an isotropic approximation $\mathbb{C}^{eff,iso}$ (Browaeys and Chevrot, 2004), optimal w.r.t. the Euclidean norm on the Voigt matrix representation of the elastic tensor. In this way, we can talk about effective elastic moduli, Poisson's ratios and isotropic approximation errors.

5.2. Comparison of μ XRCT images to generated structures

5.2.1. Simulations based on μ XRCT scans

In a first step, we wish to assess if the generated structures lead to effective elastic properties comparable to those of the μ XRCT specimen, cf. Fig. 13. On the μ XRCT image, sand grains and binder cannot be distinguished. Thus, we furnish both the μ XRCT image and both the sand as well as the binder phases of the generated microstructures with fictitious elastic constants, and compare the effective properties. As the elastic properties of sand and binder are of the same order of magnitude (for dry climate conditions), this should give a good impression on the usefulness of the computer generated structures. For $E = 100$ GPa and $\nu = 0.17$ effective elastic tensors of the 64 subsamples of the scan (cropped to 375^3 voxels) were computed, see Fig. 5(b) for the distribution of the computed values. The smallest Young's modulus was 8.39 GPa, which corresponds to the on subsample with a total solid volume fraction below 5%, cf. Fig. 5(a). The average computed Young's modulus was 11.38 GPa with a standard deviation of 0.87 GPa. At 11.46 GPa, the median is very close to the average.

5.2.2. Resolution study

A resolution study serves as the starting point of our parameter sensitivity investigation. We consider a microstructure containing 64^3 sand grains of particle 1 (Fig. 7(a)) with a volume fraction of 58.41% and a binder volume fraction of 1.10%, initially resolved by

Table 5
Results for the resolution study of Section 5.2.2.

Resolution	Young's modulus E [GPa]	Poisson's ratio ν	Isotropic approximation error [%]
64^3	10.87	0.167	12.25
128^3	10.65	0.162	9.43
256^3	10.87	0.160	8.78
512^3	10.91	0.160	8.55

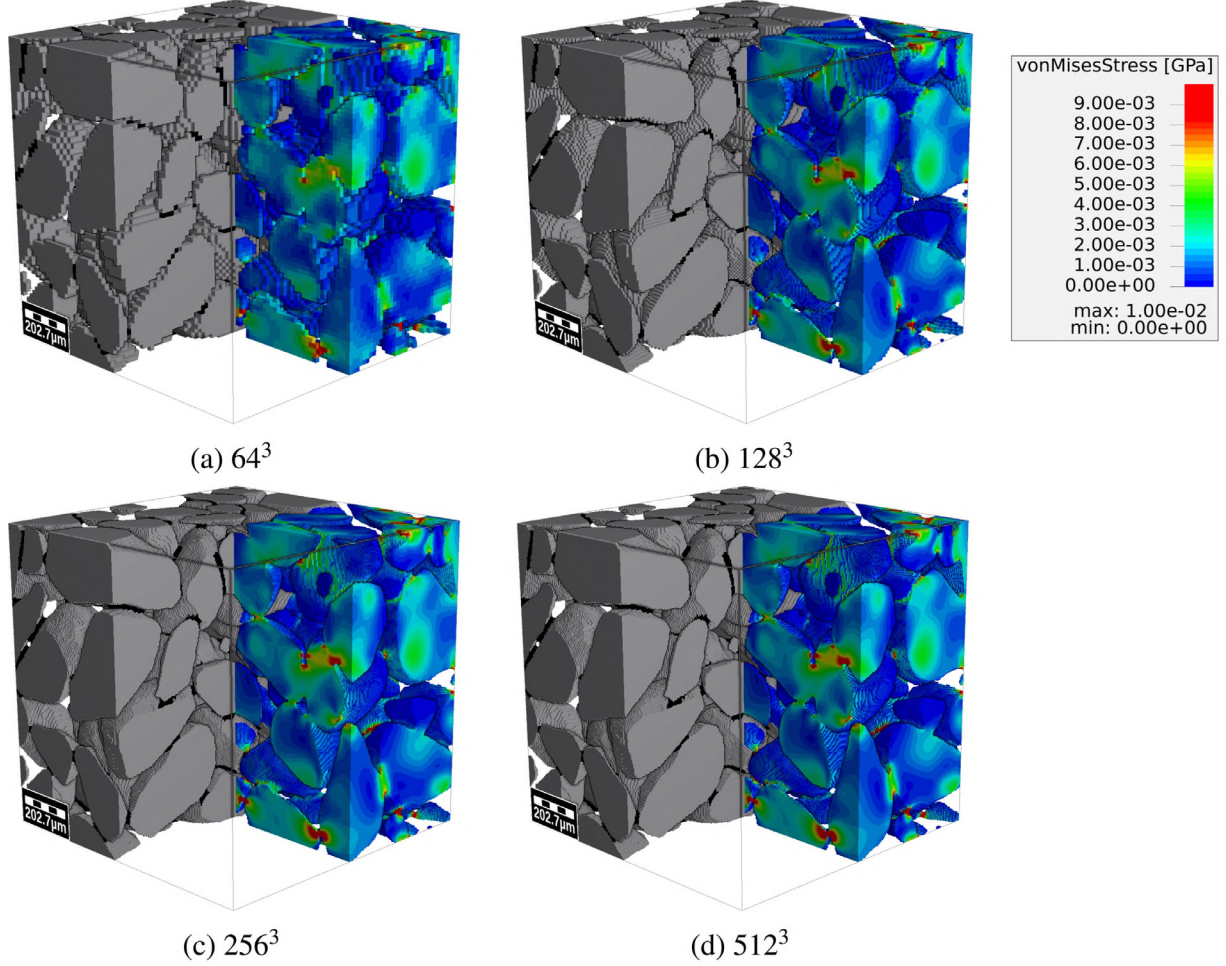


Fig. 14. Microstructure and local von Mises equivalent stress fields for 0.5% extension in e_x -direction, $64 = 4^3$ grains.

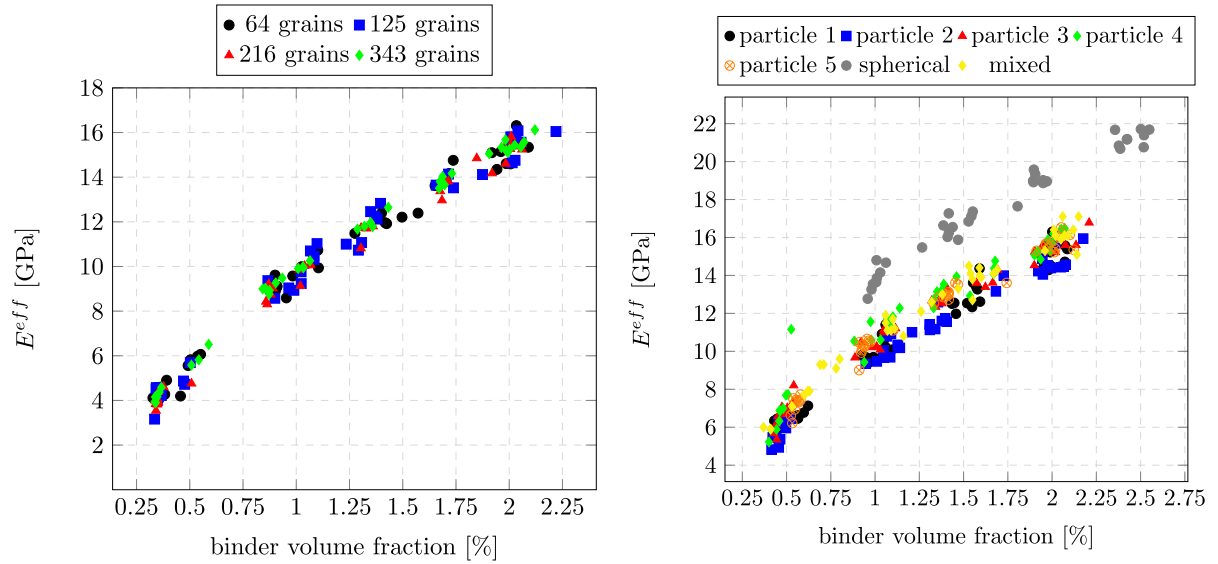
256^3 cubical voxels with dimension $3.8\mu\text{m}$. This initial structure was down-sampled by factors of 2^3 and 4^3 , and up-sampled by a factor of 2^3 , and the effective elastic tensors of these four structures was computed, see Table 5.

The computed effective elastic parameters differ only insignificantly for this particular microstructure. However, the isotropic approximation error decreases by increasing the resolution. These two observations mean that for a coarse resolution, the effective elastic properties become more anisotropic, yet the (orientation) average remains similar to the high resolution counterpart. Of course, the isotropic approximation error does not become negligible as one cannot expect isotropy for a 64 particle ensemble. Taking a look at the local stress fields, cf. Fig. 14, shows that not all stress concentrations are captured on the coarsest scale. There is, however, no large difference between the fields for 128^3 , 256^3 and 512^3 voxels, respectively. Thus, we conclude that a downsampling of the structure by a factor of 2 in each coordinate direction leads to results sufficiently accurate for our purposes.

5.3. Influence of the number of grains in the microstructure

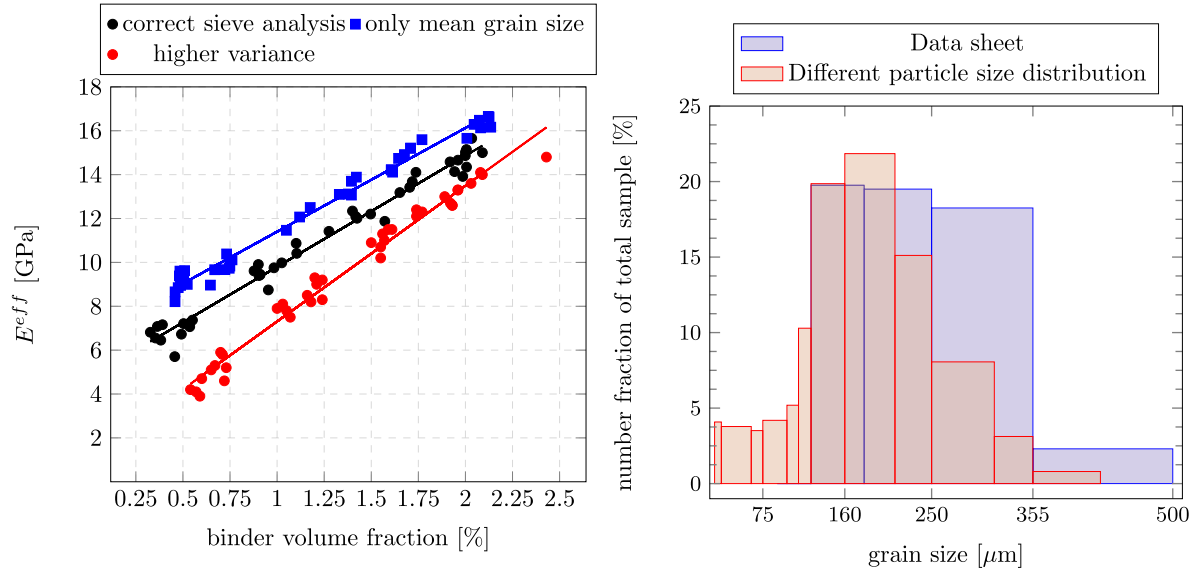
We study the influence of the number of grains in the granular packing on the effective Young's modulus. For this purpose, packings with $4^3 = 64$, $5^3 = 125$, $6^3 = 216$ and $7^3 = 343$ re-scaled copies of particle 1 were prepared as explained in Section 4, for 10 realizations. Binder was added with 0.5%, 1%, 1.5% and 2%. The computations were carried out for 128^3 (64 grains), 160^3 (125 grains), 192^3 (216 grains) and 224^3 (343 grains) voxels, each with a resolution of about $8\mu\text{m}$.

The computed effective elastic moduli are shown in Fig. 15(a). The plot emphasizes the scattering caused by the inaccuracies of the morphology-based scheme to add binder. Apparently, in the regime considered, the effective modulus of elasticity is approximately a linear function of the added binder. Surprisingly, increasing the number of grains does neither decrease the variance of the resulting binder volume fraction nor does it change the shape of the modulus of elasticity-binder volume fraction relationship. The latter phenomenon is rooted in our use of quasirandom numbers



(a) Effective Young's modulus for different grain numbers and different binder fractions

(b) Effective Young's modulus for different grain shapes and different binder fractions



(c) Effective Young's modulus for monodisperse and polydisperse packings

(d) Grain size distributions used for (c).

Fig. 15. Studies on the influence of grain number, grain shape and the particle size distribution on the effective modulus of elasticity.

Table 6

Seven microstructures which fit the computational results of the μ XRCT image best.

	A	B	C	D	E	F	G
number of grains	64	216	216	216	216	343	343
sand volume fraction	58.58	58.60	58.60	58.58	58.58	58.57	58.57
binder volume fraction	1.28	1.33	1.36	1.36	1.30	1.29	1.32
resolution	128 ³	192 ³	192 ³	192 ³	192 ³	224 ³	224 ³
E^{eff} [GPa]	11.42	11.78	11.67	11.76	11.52	11.69	11.70

for selecting the particle sizes. With these results in hand, we stick to $4^3 = 64$ grains for our further studies.

5.4. Influence of the particle shape

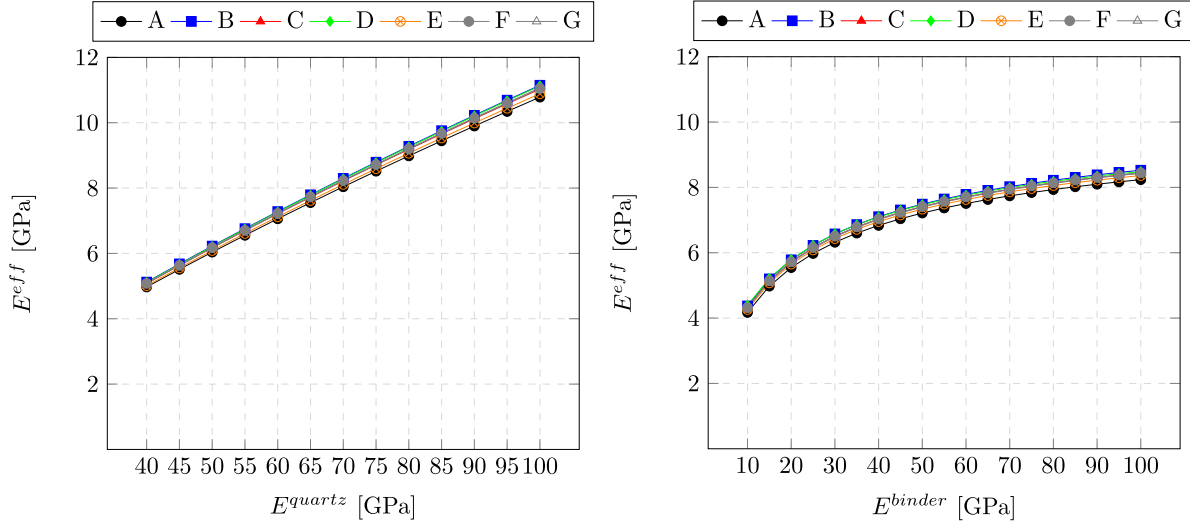
To study the influence of the grain shape, we prepared granular packs with all five particles shown in Fig. 7, and, addition-

ally, spherically-shaped grains. For each particle shape, 64 grains were packed according to the sieve analysis of Fig. 2, 10 realizations each. To each of these 60 microstructures, 0.5%, 1%, 1.5% and 2% volume fraction of binder was added. The results of the computational homogenization on these 240 128^3 microstructures can be read from Fig. 15(b). We see that the particles 1, 2, 3 and 5 lead to more or less the same Young's modulus. The effective Young's

Table 7

Elastic parameters computed for the seven microstructures of Table 6 and realistic material parameters.

	A	B	C	D	E	F	G	average
H_x^{eff} [GPa]	9.04	9.41	8.59	8.26	8.52	8.85	8.66	8.76 ± 0.35
H_y^{eff} [GPa]	8.48	8.16	8.60	9.00	8.25	8.54	8.74	8.54 ± 0.26
H_z^{eff} [GPa]	7.94	8.88	8.76	8.95	8.95	8.70	8.49	8.67 ± 0.33
E^{eff} [GPa]	7.78	8.06	7.98	8.03	7.90	7.98	7.96	7.96 ± 0.09
ν^{eff}	0.183	0.182	0.181	0.181	0.180	0.179	0.181	0.181 ± 0.001
err _{iso} [%]	6.55	6.71	3.82	4.25	3.72	3.73	3.61	

(a) Variation sand, $E^{binder} = 71.7$ GPa(b) Variation binder, $E^{sand} = 66.9$ GPa**Fig. 16.** Variation of the Young's moduli of binder and sand.

moduli of particles 1 and 2 are almost identical, and particles 3–5 induce slightly larger Young's moduli. Notice, for comparison, that spherical particles lead to a much higher effective Young's modulus. For instance, at 1% binder volume fraction, particle 1 leads to $E \approx 10$ GPa, whereas spherical particles lead to $E \approx 14$ GPa, which is an increase of about 40%. For the “correct” binder volume fraction of 1.2% the structures generated on the basis of the grain shapes extracted from the μ XRCT image are very close to the μ XRCT image results. Using spherical particles, on the other hand, lead to Young's moduli which are 20–40% too high, and the values of the μ XRCT image cannot be reproduced in that way. Last but not least we have carried out simulations where all five particles shapes are mixed at equal portions, termed “mixed” in Fig. 15(b). The resulting Young's modulus coincides with the predictions using only a single grain shape.

5.5. Influence of the particle size distribution

We compare our previous results to 10 packed structures with 64 particles of template 1, each of which is identical in size. In Fig. 15(c) we see that monodisperse packings lead to a severely higher effective Young's modulus, by about 20%. Furthermore, we compare to another particle size distribution which has the same mean grain size, but a higher variance, cf. Fig. 15(d), also with 64 particles of template 1. We see that a higher variance in the grain size leads to a lower effective Young's modulus. The latter phenomenon is easy to explain: Grain size distributions with higher variance also have a higher volume fraction at which they reach their maximally jammed state. So suppose variant A reaches a higher volume fraction than variant B. If both are rescaled to some fixed (lower) volume fraction, then the average distance between

the particles for A is higher than for B. Thus, if we further add binder, the contact area between the grains in A will be smaller than for B, too. Thus, A will have lower Young's modulus.

5.6. Best fitting microstructures

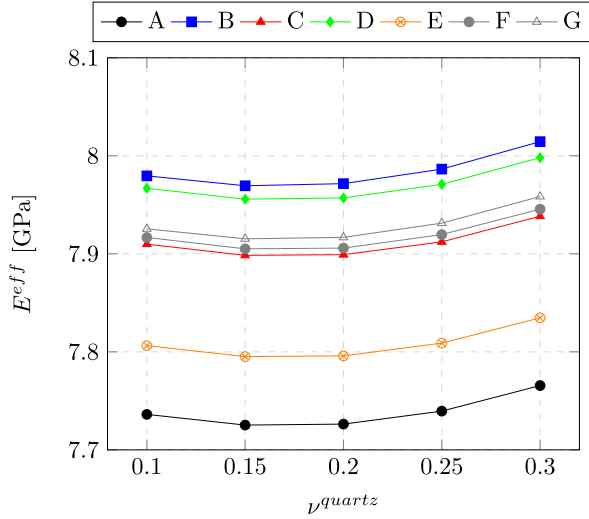
From the microstructures generated with particle 1 as the template we have selected 7 microstructures which fit the computed average modulus of elasticity 11.38 GPa based on the μ XRCT images best. We label these structures from A to G. Their properties are listed in Table 6.

6. Parameter variation

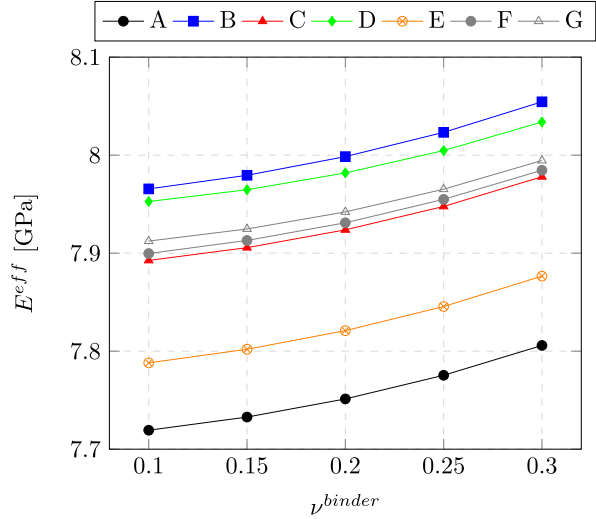
6.1. Setup

The seven microstructures identified in the previous section serve as our working horses for studying the influence of the elastic parameters on the constituents. Recall that - due to their chemical similarity - we could not distinguish binder and sand grains on the μ XRCT image. However, for our identified structures we can vary both the Young's modulus and Poisson's ratio for the two phases individually.

Following Daphalapurkar et al. (2011) we use a Young's modulus of 66.9 GPa as the reference value for the quartz sand, and vary around a Poisson's ratio of 0.25, cf. Wichtmann and Triantafyllidis (2010). Getting hands on elastic moduli of potassium silicate is much harder. Thus we use quartz glass as a reference, $E = 71.7$, $\nu = 0.17$ Sanditov et al. (2009), but take into account a large variation of these moduli. The computed effective elastic constants for the 7 microstructures can be read from Table 7.

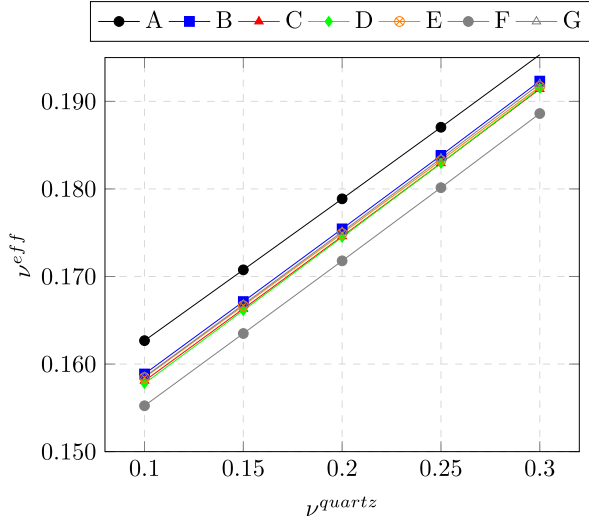


(a) Variation quartz ν , $E^{binder} = 71.7$ GPa

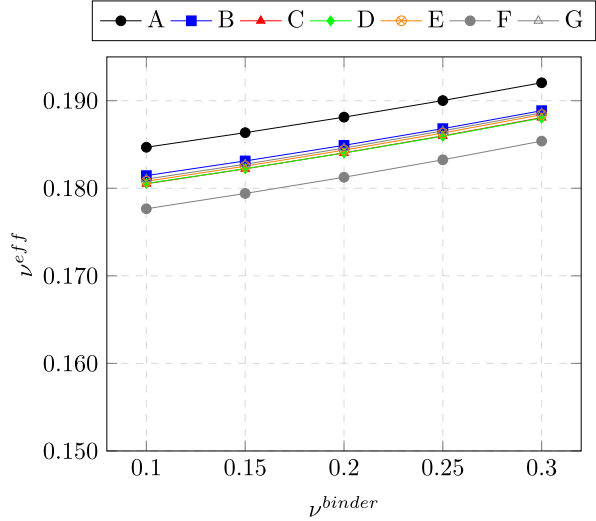


(b) Variation binder ν , $E^{sand} = 66.9$ GPa

Fig. 17. Variation of the Poisson's ratio of binder and sand 64^3 voxels, plotted: E .



(a) Variation quartz ν , $E^{binder} = 71.7$ GPa



(b) Variation binder ν , $E^{sand} = 66.9$ GPa

Fig. 18. Variation of the Poisson's ratio of binder and sand 64^3 voxels, plotted: ν .

We see that the standard deviation of Young's modulus is smaller by a factor of 3 to 4 compared to the standard deviation of the P -wave moduli. This is consistent with our resolution study, an isotropic approximation reduces the variance significantly. Compared to the measurements of Table 3, the average computed P -wave modulus of 8.66 GPa overestimates the measured average of 8.12 GPa by 6.6%. A similar trend is observed for the Young's modulus, which is overestimated by 5.4%.

6.2. Variation of Young's modulus

First we fix all elastic constants but the Young's modulus of the quartz sand, which we vary between 40 GPa and 100 GPa, which is a typical range for measured Young's moduli of quartz sand grains (Daphalapurkar et al., 2011). The effective Young's modulus varies linearly between 5 GPa and 10.8 GPa, with almost no differences between the 7 structures. Typically, quartz sand is not solely composed of quartz, but often the elastic parameters of pure quartz,

which lie between 80 and 100 GPa, are used for modelling quartz sand. Fig. 16(a) quantifies the consequences. In the regime considered, the effective Young's modulus is an affine linear function of the Young's modulus of the sand grains.

Secondly, we vary the binder's modulus of elasticity between 10 GPa and 100 GPa. The resulting curve, cf. Fig. 16(b), is roughly square-root-shaped. In particular, if the binder's Young's modulus is not too small, the effect of changing the binder's modulus of elasticity is not dramatic. In particular, in the region between 50 and 80 GPa (Pedone et al., 2007), which we consider a realistic range for E^{binder} (dry state), E^{eff} computes in the interval [7.27, 8.12] GPa, which is in line with the experimental data. We furthermore observe that for small E^{binder} the effective Young's modulus becomes small very quickly. In particular, as increasing humidity dramatically decreases the stiffness of waterglass (and influences E^{sand} insignificantly), also the effective elastic properties of the sand core composite decrease drastically.

6.3. Variation of Poisson's ratio

Poisson's ratio of quartz sand and waterglass are difficult to determine experimentally. Thus, we choose to work with only rough approximations. In this section, we examine the dependence of the effective isotropic elastic constants on the Poisson's ratio of the two micro-constituents.

First, we vary Poisson's ratio of the sand grains. The effective Young's modulus, cf. Fig. 17(a), only changes slightly. Indeed, the differences between the 7 microstructures dominate the changes induced by varying ν^{sand} , ν^{eff} , on the other hand, changes linearly with ν^{binder} , cf. Fig. 18(a). Thus, we conclude that changing Poisson's ratio of the sand grains only changes the effective Poisson's ratio, but does not have a significant effect on the effective modulus of elasticity. Similar conclusions hold for varying ν^{binder} , see Figs. 17(b) and 18(b), but the influence on the effective properties is much smaller.

7. Conclusions

In this work we have modelled the microstructure of chemically bonded quartz sand cores by combining a packing algorithm with mathematical morphological operations to insert the binder bridges. These microstructures, which share the same statistical properties and the same complexity as the μ XRCT scan, but permit distinguishing binder and sand grains, served as the input for FFT-based computational homogenization, leading to computed effective elastic constants which turned out to be close to P -wave measurements.

Most importantly, it would be desirable to have means for measuring the elastic properties of the binder. However, due to the curing process and the induced nanostructure the "effective" elastic constants of the binder appear not to be material properties, but, rather, are outcomes of the processing condition during curing and the local arrangement of the sand grains. These difficulties are subject to current research, which was unavailable during the writing of this article, but will be published in the near future. Still, there is a good agreement between measured and computed elastic properties, and it would be interesting whether the method developed in this article can be applied to other compositions of sand cores, i.e. if the sieve line or the sand type is varied, or the binding agent changes. Furthermore investigating the strength properties of the compound, can be tackled.

From a methodological perspective it is satisfying to see that this type of homogenization problem can be tackled - despite all apparent complexity. In particular, the chosen sand grain shape had little influence, and the "representative volume" turned out to be unexpectedly small. We attribute this amazing simplicity to the core blowing process itself (which we model by the packing algorithm): due to the high packing density, the apparent chaos becomes ordered. For instance, two sand grain shapes appear different at first. However, when compacted, their differences shrink because of the rearrangement induced by the packing. Of course, something like the average number of nearest-neighbor-contacts plays an important role, explaining the differences between spherical and realistic grain shapes (Fig. 15(b)). However, the randomly chosen five particles appear to be similar in this regard.

Concerning efficiency the most time consuming step at the moment is the coating of each individual particle. This limitation might be overcome by more intelligent algorithms.

Acknowledgements

This research was supported by DFG projects AN 341/9-1 and VO 1487/16-1.

We thank Quarzwerke GmbH and ASK Chemicals GmbH for providing the necessary materials. M.S. thanks the Fraunhofer ITWM for its hospitality during the writing of this article. We thank Franz Schreiber (Department of image processing, Fraunhofer ITWM Kaiserslautern) for providing the μ XRCT-scans, and Matthias Kabel as well as Torben Prill for stimulating discussions.

References

- Anthony, J.W., 1990. Handbook of Mineralogy. Mineral Data Publishing, Tucson, Ariz., USA.
- Bakhtiyarov, S.I., Sherwin, C.H., Overfelt, R.A., 2007. Untersuchung des Heißverzugs von Phenolurethan Cold-Box Kernen [Investigation of the hot delay of phenolurethan cold box cores]. *Giesserei-Praxis* 1–2, 12–21.
- Barrios, G.K.P., de Carvalho, R.M., Kwade, A., Tavares, L.M., 2013. Contact parameter estimation for DEM simulation of iron ore pellet handling. *Powder Technol.* 248, 84–93.
- Bennet, C.H., 1972. Serially deposited amorphous aggregates of hard spheres. *J. Appl. Phys.* 43 (6), 2727–2734.
- Blair, M., Stevens, T.L., 1995. *Steel Castings Handbook*. ASM International, Russell Township, USA.
- Brisard, S., Dormieux, L., 2010. FFT-based methods for the mechanics of composites: a general variational framework. *Comput. Mater. Sci.* 49 (3), 663–671.
- Brisard, S., Dormieux, L., 2012. Combining Galerkin approximation techniques with the principle of Hashin and Shtrikman to derive a new FFT-based numerical method for the homogenization of composites. *Comput. Methods Appl. Mech. Eng.* 217–220, 197–212.
- Browaeys, J.T., Chevrot, S., 2004. Decomposition of the elastic tensor and geophysical applications. *Geophys. J. Int.* 159, 667–678.
- Caylak, I., Mahnken, R., 2010. Thermomechanical characterisation of cold box sand including optical measurements. *Int. J. Cast Met. Res.* 23 (3), 176–184.
- Cnudde, V., Boone, M.N., 2013. High-resolution X-ray computed tomography in geosciences: a review of the current technology and applications. *Earth Sci. Rev.* 123, 1–17.
- Coelho, D., Thovert, J.-F., Adler, P.M., 1997. Geometrical and transport properties of random packings of spheres and aspherical particles. *Phys. Rev. E* 55, 1959–1978.
- Cundall, P.A., 1988a. Formulation of a three-dimensional distinct element model—Part I: A Scheme to detect and represent contacts in a system composed of many polyhedral blocks. *Int. J. Rock Mech.* 25 (3), 107–116.
- Cundall, P.A., 1988b. Formulation of a three-dimensional distinct element model—Part II: mechanical calculations for motion and interaction of a system composed of many polyhedral blocks. *Int. J. Rock Mech.* 25 (3), 117–125.
- Damasceno, P.F., Engel, M., Glotzer, S.C., 2012. Predictive self-assembly of polyhedra into complex structures. *Science* 337, 6093.
- Daphalapurkar, N.P., Wang, F., Fu, B., Lu, H., Komanduri, R., 2011. Determination of mechanical properties of sand grains by nanoindentation. *Exp. Mech.* 51, 719–728.
- Dick, J., Pillichshammer, F., 2010. *Digital Nets and Sequences. Discrepancy Theory and Quasi-Monte Carlo Integration*. Cambridge University Press, Cambridge, UK.
- Favier, J.F., Abbaspour-Fard, M.H., Kremmer, M., Raji, A.O., 1999. Shape representation of axis-symmetrical, non-spherical particles in discrete element simulation using multi-element model particles. *Eng. Comput.* 16, 467–480.
- Ferrellec, J.-F., McDowell, G.R., 2008. A simple method to create complex particle shapes for DEM. *Geomech. Geoeng.* 3 (3), 211–216.
- Finite elements for elastic materials and homogenization, (FeelMath). Fraunhofer ITWM, <http://www.itwm.fraunhofer.de/en/departments/flow-and-material-simulation/mechanics-of-materials/feelmath.html>, Kaiserslautern, Germany Accessed: 09-01, 2017.
- Garcia, X., 2009. Numerical Modelling of the Microstructure and Permeability of Granular Materials. Imperial College London Ph.D. thesis.
- Garcia, X., Latham, J.-P., Xiang, J., Harrison, J., 2009. A clustered overlapping sphere algorithm to represent real particles in discrete element modelling. *Geotechnique* 59 (9), 779–784.
- GeoDict, Math2Market GmbH, Kaiserslautern, Germany. Accessed: -09-01 <http://www.geodict.de>. 2017.
- Gerritsma, M.I., 1996. Time Dependent Numerical Simulations of a Viscoelastic Fluid on a Staggered Grid. Rijksuniversiteit Groningen Ph.D. thesis.
- Greenwood, N.N., Earnshaw, A., 1997. *Chemistry of the Elements*. Butterworth-Heinemann, Oxford, UK.
- Griebel, B., Brecheisen, D., Ramakrishnan, R., Volk, W., 2016. Optical measurement techniques determine Young's modulus of sand core materials. *Int. J. Metalcast.* 10 (4), 524–530.
- Güven, I., Luding, S., Steeb, H., 2017. Incoherent waves in fluid-saturated sintered granular systems: scattering phenomena. *ASME. J. Vib. Acoust.* 140 (1), 011018–011018–7.
- Harlow, F.H., Welch, J.E., 1965. Numerical calculation of time-dependent viscous incompressible flow of fluid with free surface. *Phys. Fluids* 8, 2182–2189.
- Heitkam, S., Drenckhan, W., Fröhlich, J., 2012. Packing spheres tightly: influence of mechanical stability on close-packed sphere structures. *Phys. Rev. Lett.* 108, 148–302.
- Henzie, J., Grünwald, M., Widmer-Cooper, A., Geissler, P.L., Yang, P., 2012. Selfassembly of uniform polyhedral silver nanocrystals into densest packings and exotic superlattices. *Nat. Mater.* 11, 131–137.

- Hirano, T., Usami, K., Tanaka, Y., Masuda, C., 1995. In situ X-ray CT under tensile loading using synchrotron radiation. *J. Mater. Res.* 10 (2), 381–386.
- Hogue, C., Newland, D., 1994. Efficient computer simulation of moving granular particles. *Powder Technol.* 78 (1), 51–66.
- Höhner, D., Wirtz, S., Kruggel-Emden, H., Scherer, V., 2010. Comparison of the multi-sphere and polyhedral approach to simulate non-spherical particles within the discrete element method: influence on temporal force evolution for multiple contacts. *Phys. Rev. E* 229 (9), 3295–3315.
- Holister, S., Kikuchi, N., 1994. Homogenization theory and digital imaging: a basis for studying the mechanics and design principles of one tissue. *Biotech. Bioeng.* 43, 586–596.
- Houlsby, G.T., 2009. Potential particles: a method for modelling non-circular particles in DEM. *Comput. Geotech.* 36 (6), 953–959.
- Iden, F., Pohlmann, U., Tilch, W., Wojtas, H.-J., 2011a. Strukturen von Cold-Box-Bindersystemen und die Möglichkeit ihrer Veränderung [Structures of Cold Box Binder Systems and the Possibility of influencing them]. *Giesserei-Rundschau* 58, 3–8.
- Iden, F., Tilch, W., Wojtas, H.-J., 2011b. Der Sand als Einflussfaktor auf die kern- und gießtechnischen Eigenschaften von Cold-Box-Kernen [On the impact of the mold sand on the properties of cold box cores]. *Giesserei* 98, 18–25.
- Jia, X., Gopinathan, N., Williams, R.A., 2002. Modeling complex packing structures and their thermal properties. *Adv. Powder Technol.* 13 (1), 55–71.
- Leavers, V.F., 1998. Shape representation and contact detection for discrete element simulations of arbitrary geometries. *Eng. Comput.* 15 (3), 374–390.
- Leavers, V.F., 2000. Use of the two-dimensional radon transform to generate a taxonomy of shape for the characterization of abrasive powder particles. *IEEE Trans. Pattern Anal. Mach. Intell.* 22 (12), 1411–1423.
- Ledbetter, H.M., 1981. Elastic constants of polycrystalline copper at low temperatures. relationship to single-crystal elastic constants. *Physica Status Solidi (a)* 66 (2), 477–484.
- Lee, J., Santamarina, J., 2005. Bender elements: performance and signal interpretation. *J. Geotech. Geoenviron. Eng.* 131 (9), 1063–1070.
- Li, C.-Q., Xua, W.-J., Meng, Q.-S., 2015. Multi-sphere approximation of real particles for DEM simulation based on a modified greedy heuristic algorithm. *Geomech. Geoenviron. Eng.* 286, 478–487.
- Maggi, F., Stafford, S., Jackson, T.L., Buckmaster, J., 2008. Nature of packs used in propellant modeling. *Phys. Rev. E* 77, 046107.
- Marcotte, E., Torquato, S., 2013. Efficient linear programming algorithm to generate the densest lattice sphere packings. *Phys. Rev. E* 87, 063303.
- Mollon, G., Zhao, J., 2013. Generating realistic 3D sand particles using Fourier descriptors. *Granul. Matter* 15 (1), 95–108.
- Moulinec, H., Suquet, P., 1994. A fast numerical method for computing the linear and nonlinear mechanical properties of composites. *C. R. Acad. Sci. Ser. II* 318 (11), 1417–1423.
- Moulinec, H., Suquet, P., 1998. A numerical method for computing the overall response of nonlinear composites with complex microstructure. *Comput. Methods Appl. Mech. Eng.* 157, 69–94.
- Nolan, G.T., Kavanagh, P.E., 1992. Computer simulation of random packing of hard spheres. *Powder Technol.* 72, 149–155.
- Ohser, J., Mücklich, F., 2000. Statistical analysis of microstructures in materials science. John Wiley, Hoboken, USA.
- Ohser, J., Schladitz, K., 2009. 3D Images of Materials Structures: Processing and Analysis. Wiley-VCH, Weinheim, Germany.
- O'Sullivan, C., 2011. Particle-based discrete element modeling: geomechanics perspective. *Int. J. Geomech.* 11 (6), 449–464.
- Otsu, N., 1979. A threshold selection method from gray-level histograms. *IEEE Trans. Syst. 9* (1), 62–66.
- Pedone, A., Malavasi, G., Cormack, A.N., Segre, U., Menziani, M.C., 2007. Insight into elastic properties of binary alkali silicate glasses; prediction and interpretation through atomistic simulation techniques. *Chem. Mater.* 19 (13), 3144–3154.
- Polzin, H., 2012. Anorganische Binder: zur Form und Kernherstellung in der Gießerei. Schiele & Schoen, Berlin, Germany.
- Rao, T.V., 2003. Metal Casting: Principles and Practice. New Age International, New Delhi, India.
- Rowe, R.C., York, P., Colbourn, E.A., Roskilly, S.J., 2005. The influence of pellet shape, size and distribution on capsule filling-A preliminary evaluation of three-dimensional computer simulation using a Monte-Carlo technique. *Int. J. Pharm.* 300 (1), 32–37.
- Sanditov, D.S., Mantatov, V.V., Sanditov, B.D., 2009. Poisson ratio and plasticity of glasses. *Tech. Phys.* 54 (4), 594–596.
- Schneider, M., Merkert, D., Kabel, M., 2016. FFT-based homogenization for microstructures discretized by linear hexahedral elements. *Int. J. Numer. Methods Eng.* Accepted for publication and available online. 1–29.
- Schneider, M., Ospald, F., Kabel, M., 2016. Computational homogenization of elasticity on a staggered grid. *Int. J. Numer. Methods Eng.* 105 (9), 693–720.
- Sobol, I.M., 1967. Distribution of points in a cube and approximate evaluation of integrals. *U.S.S.R Comput. Maths. Math. Phys.* 7, 86–112.
- Sonon, B., François, B., Massart, T., 2012. A unified level set based methodology for fast generation of complex microstructural multi-phase RVEs. *Comp. Methods Appl. Mech. Eng.* 223, 103–122.
- Stafford, S., Jackson, T.L., 2010. Using level sets for creating virtual random packs of non-spherical convex shapes. *Phys. Rev. E* 229 (9), 3295–3315.
- Stillinger, F.H., Lubachevsky, B.D., 1993. Crystalline-amorphous interface packings for disks and spheres. *J. Stat. Phys.* 73, 497–514.
- Torquato, S., Jiao, Y., 2009. Dense packings of polyhedra: platonic and archimedean solids. *Phys. Rev. E* 80, 041104.
- Torquato, S., Jiao, Y., 2010. Robust algorithm to generate a diverse class of dense disordered and ordered sphere packings via linear programming. *Phys. Rev. E* 82, 061302.
- Wichtmann, T., Triantafyllidis, T., 2009. On the influence of the grain size distribution curve of quartz sand on the small strain shear modulus G_{max} . *J. Geotech. Geoenviron. Eng.* 135 (10), 1404–1418.
- Wichtmann, T., Triantafyllidis, T., 2010. On the influence of the grain size distribution curve on P-wave velocity, constrained elastic modulus M_{max} and Poisson's ratio of quartz sands. *Soil Dyn. Earthq. Eng.* 30 (8), 757–766.
- Williams, J.R., O'Connor, R., 1999. Discrete element simulation and the contact problem. *Arch. Comput. Methods Eng.* 6 (4), 279–304.
- Williams, S., Philipse, A., 2003. Random packings of spheres and spherocylinders simulated by mechanical contraction. *Phys. Rev. E* 67, 1–9.
- Willot, F., 2015. Fourier-based schemes for computing the mechanical response of composites with accurate local fields. *Comptes Rendus - Mécanique* 343 (3), 232–245.
- Willen, C.S., Lu, N., Likos, W.J., 2012. Quantification of grain, pore and fluid microstructure of unsaturated sand from X-ray computed tomography images. *Geotech. Test. J.* 35 (6), 1–13.
- Zeman, J., Vondřejc, J., Novák, J., Marek, I., 2010. Accelerating a FFT-based solver for numerical homogenization of periodic media by conjugate gradients. *J. Comput. Phys.* 229 (21), 8065–8071.